

Realizing the Petz Recovery Map on an NMR Quantum Processor

Gayatri Singh,¹ Ram Sagar Sahani,¹ Vinayak Jagadish,^{2,3} Lea Lautenbacher,⁴ Nadja K. Bernardes,⁵ and Kavita Dorai¹

¹*Department of Physical Sciences, Indian Institute of Science Education & Research Mohali, Sector 81 SAS Nagar, Manauli PO 140306 Punjab India*

²*Centre for Quantum Science and Technology, Chennai Institute of Technology, Chennai, 600069, India*

³*National Institute for Theoretical and Computational Sciences (NITheCS), Stellenbosch, 7600, South Africa*

⁴*Institut für Theoretische Physik, Albert-Einstein-Allee 11, Universität Ulm, D-89069 Ulm, Germany*

⁵*Departamento de Física, Universidade Federal de Pernambuco, Recife, PE 50670-901 Brasil*

The Petz recovery map is a fundamental protocol in quantum information theory, enabling the retrieval of quantum information lost due to noisy processes. Here, we experimentally implement the Petz recovery map on a nuclear magnetic resonance (NMR) quantum processor using the duality quantum computing (DQC) algorithm. Focusing on two paradigmatic single-qubit channels, namely phase damping and amplitude damping, we demonstrate that the recovered states closely match theoretical predictions. Our results validate the feasibility of the Petz-based recovery map in current quantum platforms and highlight its relevance for near-term error mitigation strategies.

I. INTRODUCTION

Open quantum systems [1, 2] are defined by their interaction with an external environment, which breaks the idealization of a perfectly isolated/closed quantum system. While classical systems can exchange energy with their surroundings in a straightforward manner, quantum systems exhibit a far more delicate sensitivity to environmental interactions. This sensitivity manifests in phenomena such as decoherence, wherein a quantum system initially in a pure state evolves into a statistical mixture due to the build-up of entanglement with the environment. Decoherence is particularly detrimental to quantum technologies, as it erodes the fundamental quantum properties, namely superposition and entanglement, that underpin quantum computing, communication, sensing etc. [3–8].

Mathematically, the process of decoherence can be understood through the lens of quantum channels, which describe the dynamics of the quantum system of interest under noise. For instance, a dephasing channel suppresses off-diagonal elements of the density matrix, effectively randomizing quantum phases, while an amplitude damping channel models energy dissipation, such as spontaneous emission in atomic systems. These noise processes are not merely theoretical constructs; they are omnipresent in experimental platforms, from superconducting qubits to trapped ions and NMR systems [9–11].

To counteract decoherence effects and information loss in quantum systems, a variety of error mitigation and correction techniques have been developed. Among the general strategies proposed for recovering quantum information, the Petz recovery map stands out as a particularly elegant and general approach, grounded in quantum information theory [12, 13]. It provides a mathematically well-defined prescription for approximately inverting the action of a noisy quantum channel, conditioned on partial knowledge of the dynamics of the system of interest. Beyond its theoretical importance, the Petz map finds

utility in quantum error correction, tomography, black hole physics, where information seems to be lost but may yet be retrievable, quantum resource theories, and quantum thermodynamics [14–18]. Until recently, the Petz recovery map remained primarily a theoretical construct, with no direct experimental realization. Recently, an implementation of the Petz map in trapped-ion platforms has been achieved [19], marking a step toward its practical realization. In parallel, algorithmic approaches have been developed to embed the Petz recovery channel within quantum circuits [20], and noise-adapted recovery strategies inspired by the Petz map have been designed to achieve near-optimal fidelity for arbitrary quantum codes and noise models [21].

The central goal of this work is to bridge the gap between the theoretical foundations of the Petz recovery map and its practical implementation in realistic quantum settings. We propose an experimental realization of Petz maps using NMR techniques. Building on the detailed theoretical analyses of the Petz map under physically relevant noise models [22, 23], we focus on two paradigmatic channels, dephasing and amplitude damping, which are both theoretically well understood and naturally realized in NMR platforms. Our experimental results show excellent agreement with theoretical predictions, providing not only a compelling validation for the physical implementability of Petz recovery, but also establishing a practical framework for its deployment in real-world quantum protocols. In the NMR simulation of the dynamics, the DQC algorithm [24] is employed.

This paper is structured as follows. We begin by introducing the theoretical background of quantum channels and the Petz map. We then outline the quantum channels and the experimental setup used in our NMR implementation. Our main results are followed by a detailed comparison with the theoretical predictions. Finally, we conclude with a discussion of the implications of our findings and potential future directions.

II. QUANTUM CHANNELS AND PETZ RECOVERY MAPS

The evolution of an open quantum system is described by a *quantum channel*. A quantum channel [25] is typically represented by a *completely positive, trace-preserving (CPTP)* map. Complete positivity (CP) ensures that the map maintains the positivity of quantum states when acting on a subsystem of a larger extended system, thereby preserving the physical validity of the overall state. Trace Preservation (TP) ensures that the total probability is conserved during the dynamics.

Mathematically, a quantum channel Λ is a linear map acting on the space of density matrices $\mathcal{B}(\mathcal{H})$, the space of bounded linear operators on a Hilbert space \mathcal{H} . The quantum state ρ of the system of interest transforms as

$$\rho' = \Lambda(\rho), \quad (1)$$

where ρ' is the new state after the action of the channel Λ on ρ . Quantum channels admit the *operator sum representation*, also known as the *Kraus representation*. In this representation, a quantum channel Λ is described by a set of operators $\{\mathcal{K}_m\}$, known as the *Kraus operators*,

$$\Lambda(\rho) = \sum_{m=0}^{d^2-1} \mathcal{K}_m \rho \mathcal{K}_m^\dagger, \quad (2)$$

where d is the dimension of the Hilbert space of the system. It must be noted that the Kraus representation is not unique, and is always defined up to a unitary. In the canonical representation, one could have a maximum of d^2 Kraus operators. The map is trace preserving if the set of operators $\{\mathcal{K}_m\}$ satisfy

$$\sum_m \mathcal{K}_m^\dagger \mathcal{K}_m = \mathbb{1}, \quad (3)$$

where \mathcal{K}_m^\dagger is the Hermitian conjugate of \mathcal{K}_m , and $\mathbb{1}$ is the identity operator on the Hilbert space.

Given two Hilbert spaces \mathcal{H}_A and \mathcal{H}_B , we define $S(\mathcal{H}_A)$ and $S(\mathcal{H}_B)$ as sets of density operators that act on systems A and B , respectively. A quantum channel $\Lambda: S(\mathcal{H}_A) \rightarrow S(\mathcal{H}_B)$ is said to be *reversible* if there exists a quantum channel $\mathcal{R}: S(\mathcal{H}_B) \rightarrow S(\mathcal{H}_A)$, called the *recovery channel*, such that for all density operators $\rho \in S(\mathcal{H}_A)$, the following holds:

$$(\mathcal{R} \circ \Lambda)(\rho) = \rho. \quad (4)$$

To quantify the extent to which a quantum channel affects the distinguishability of input states, we often turn to the concept of relative entropy. Under the action of a quantum channel Λ , the relative entropy between two states can never increase. This result is known as the *monotonicity of relative entropy*, or the *data processing inequality*, and is expressed as:

$$D(\Lambda(\rho) \parallel \Lambda(\sigma)) \leq D(\rho \parallel \sigma), \quad (5)$$

where $D(\rho \parallel \sigma) = \text{Tr}(\rho \log \rho) - \text{Tr}(\rho \log \sigma)$ denotes the relative entropy between the states ρ and σ .

If there exists a recovery channel \mathcal{R} such that $(\mathcal{R} \circ \Lambda)(\rho) = \rho$ and $(\mathcal{R} \circ \Lambda)(\sigma) = \sigma$, then applying monotonicity again to the channel \mathcal{R} yields the condition of equality,

$$D(\rho \parallel \sigma) = D(\Lambda(\rho) \parallel \Lambda(\sigma)). \quad (6)$$

This equality characterizes the situation where perfect recovery is possible. In fact, Petz [12, 13] identified an explicit recovery map $\mathcal{R} = \mathcal{P}_{\sigma, \Lambda}$, given by

$$\mathcal{P}_{\sigma, \Lambda}(\cdot) = \sigma^{1/2} \Lambda^\dagger \left[\Lambda(\sigma)^{-1/2}(\cdot) \Lambda(\sigma)^{-1/2} \right] \sigma^{1/2}, \quad (7)$$

where Λ^\dagger denotes the adjoint of the channel Λ and σ is the *reference state*. This recovery map $\mathcal{P}_{\sigma, \Lambda}$ is independent of the input state ρ and can be used universally for all states ρ that saturate the data processing inequality, provided that σ is full-rank to ensure the finiteness of the relative entropy.

In this work, we study the performance of the Petz map when applied to the following two quantum channels.

a. Amplitude Damping (AD) Channel: An AD channel models energy dissipation from the quantum system of interest to the environment and drives the system towards the ground state $|0\rangle$, affecting both populations and coherences of the density matrix. The action of the AD channel on a qubit can be described by the following Kraus operators:

$$\mathcal{K}_0^{AD} = \begin{pmatrix} 1 & 0 \\ 0 & \sqrt{1-p} \end{pmatrix} \quad ; \quad \mathcal{K}_1^{AD} = \begin{pmatrix} 0 & \sqrt{p} \\ 0 & 0 \end{pmatrix}, \quad (8)$$

where $p \in [0, 1]$ denotes the channel strength.

Motivated by the asymmetric nature of the AD channel, where the $|0\rangle$ state remains unaffected while the $|1\rangle$ state undergoes a probabilistic decay, we consider a parameterized reference state that is diagonal in form. With this specific choice of reference state, $\sigma = (1 - \epsilon)|0\rangle\langle 0| + \epsilon|1\rangle\langle 1|$, the corresponding Kraus operators for the Petz recovery map for AD channel are evaluated to be

$$\begin{aligned} \mathcal{M}_0^{AD} &= \begin{pmatrix} \sqrt{\frac{1-\epsilon}{1-(1-p)\epsilon}} & 0 \\ 0 & 1 \end{pmatrix} \\ \mathcal{M}_1^{AD} &= \begin{pmatrix} 0 & 0 \\ \sqrt{\frac{p\epsilon}{1-(1-p)\epsilon}} & 0 \end{pmatrix}. \end{aligned} \quad (9)$$

b. Phase Damping (PD) Channel: A PD channel causes the loss of quantum coherence by suppressing the off-diagonal elements of the density matrix of the qubit, thus erasing relative phase information between the computational basis states, without altering their populations (diagonal elements). In its Kraus representation, the PD channel on a qubit is described by

$$\mathcal{K}_0^{PD} = \sqrt{1 - \frac{p}{2}} \begin{pmatrix} 1 & 0 \\ 0 & 1 \end{pmatrix} \quad ; \quad \mathcal{K}_1^{PD} = \sqrt{\frac{p}{2}} \begin{pmatrix} 1 & 0 \\ 0 & -1 \end{pmatrix}, \quad (10)$$

where $p \in [0, 1]$ is the strength of the channel. Note that for $p = 1$ the coherences of the density matrix vanish completely. The PD channel has the most significant effect on superposition states, while it leaves diagonal states unaffected. Therefore, to construct the Petz recovery map for this channel, we consider a reference state of the form $\sigma = (1 - \epsilon)|+\rangle\langle+| + \epsilon|-\rangle\langle-|$, where $|\pm\rangle = |0\rangle \pm |1\rangle/\sqrt{2}$ are the eigenstates of the Pauli- x operator. Using this reference state, the corresponding Kraus operators for the Petz recovery map of the PD channel are given by

$$\begin{aligned} \mathcal{M}_0^{PD} &= \begin{pmatrix} \lambda_+ & \lambda_- \\ \lambda_- & \lambda_+ \end{pmatrix} \quad \text{with } \lambda_{\pm} = \sqrt{1 - \frac{p}{2}} (a\sqrt{1 - \epsilon} \pm b\sqrt{\epsilon}) \\ \mathcal{M}_1^{PD} &= \begin{pmatrix} \mu_+ & \mu_- \\ -\mu_- & -\mu_+ \end{pmatrix} \quad \text{with } \mu_{\pm} = \sqrt{\frac{p}{2}} (a\sqrt{\epsilon} \pm b\sqrt{1 - \epsilon}), \end{aligned} \quad (11)$$

where a and b are evaluated to be

$$\begin{aligned} a &= \frac{1}{\sqrt{2}\sqrt{p\epsilon + (2-p)(1-\epsilon)}} \\ b &= \frac{1}{\sqrt{2}\sqrt{p-p\epsilon + \epsilon(2-p)}}. \end{aligned}$$

III. EXPERIMENTAL DETAILS

A. Realization of NMR qubits

We used a three-qubit NMR quantum processor to experimentally realize quantum channels and their associated Petz recovery maps. The three spin-half nuclei namely, ^1H , ^{19}F , and ^{13}C , in a ^{13}C -labeled diethyl fluoromalonate molecule dissolved in acetone D6, were assigned as three individual qubits (Fig. 1(a)). All the experiments were carried out at room temperature (~ 300 K) on a Bruker Avance-III 600 MHz NMR spectrometer equipped with a 5 mm quadrupole resonance inverse (QXI) probe. The durations of $\pi/2$ pulses for ^1H , ^{19}F , and ^{13}C were $9.3\ \mu\text{s}$, $23.5\ \mu\text{s}$ and $15\ \mu\text{s}$ at power levels of $18.14\ \text{W}$, $42.47\ \text{W}$, and $179.47\ \text{W}$, respectively.

The internal Hamiltonian of the three-qubit system in the rotating frame, under the weak coupling approximation, is expressed as

$$\mathcal{H} = - \sum_{i=1}^3 (\omega_i - \omega_i^{rf}) I_{iz} + \sum_{i>j, i=1}^3 J_{ij} I_{iz} I_{jz}, \quad (12)$$

where the indices i, j label the qubits. In our case, the nuclei ^{19}F , ^1H and ^{13}C are qubits 1, 2, and 3 respectively; ω_i denotes the chemical shift, ω_i^{rf} is the rotating frame frequency, I_{iz} is the z -component of the spin angular momentum of the i th nucleus and J_{ij} is the scalar coupling between the i th and j th nuclei, with experimentally measured values : $J_{\text{CH}} = 161.42\ \text{Hz}$, $J_{\text{FH}} = 47.50\ \text{Hz}$, and $J_{\text{FC}} = -191.90\ \text{Hz}$. In NMR, the recovery of longitudinal

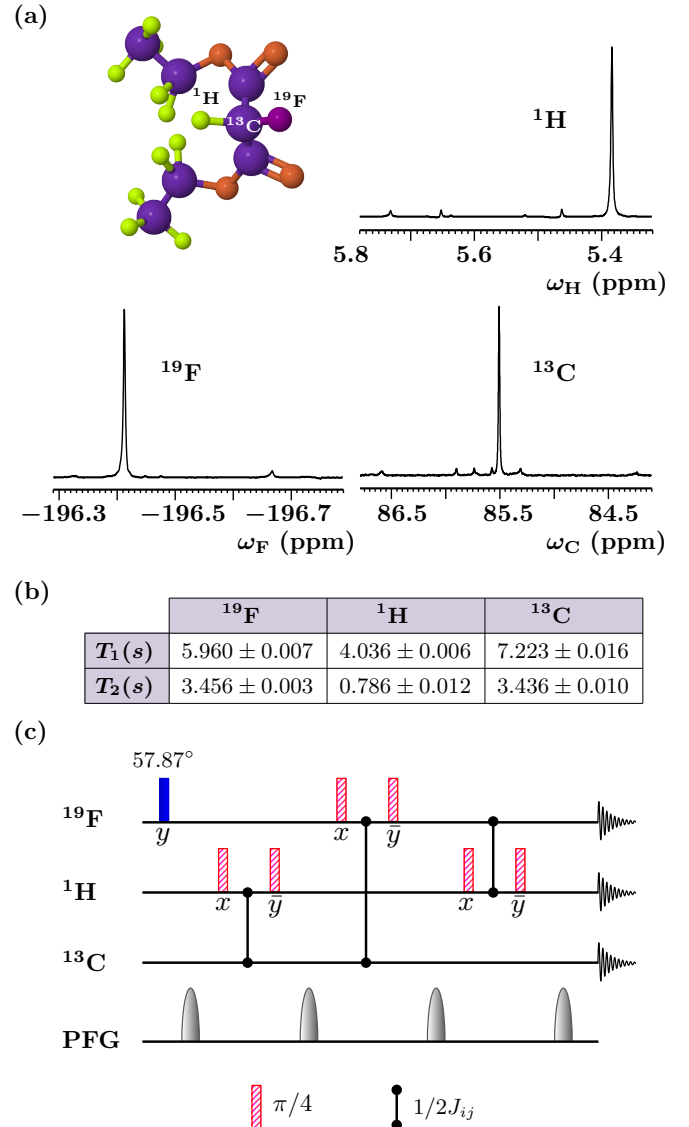


FIG. 1: (Color online) (a) The molecular structure of ^{13}C labeled diethyl fluoromalonate, used as a three-qubit system, with NMR-active nuclei ^1H , ^{19}F , and ^{13}C . The NMR spectra of the three nuclei acquired after applying a $\pi/2$ readout pulse to the PPS $|000\rangle$. The horizontal axis indicates frequency in parts per million (ppm). (b) Longitudinal relaxation (T_1) and transverse relaxation (T_2) times (in seconds) of different nuclei. (c) NMR pulse sequence for preparing the three-qubit PPS. Rectangular blocks represent RF pulses, with the flip angle and phases labeled beneath each pulse. An overbar indicates negative phase. The solid blue rectangle denotes a rotation along the y -axis by an angle 57.87° . Cross-hatched magenta rectangles denote $\pi/4$ pulses, while gray-shaded shapes indicate pulsed field gradients (PFG). A vertical line connecting two solid dots between qubits i and j indicates free evolution under the NMR Hamiltonian for a duration of $1/2J_{ij}$, where J_{ij} is the scalar J-coupling.

magnetization is characterized by the T_1 relaxation time, while the decay of transverse magnetization is governed by the T_2 relaxation time. The experimentally measured values of T_1 and T_2 relaxation times in seconds for the different nuclei given in Fig. 1(b).

We initialize our system in the pseudopure state (PPS) starting from thermal equilibrium via the spatial averaging technique [26], which comprises single qubit rotations, free evolution and pulsed field gradients (PFG). A PPS retains the spectral properties of a pure state. The NMR pulse sequence to prepare the PPS is depicted in Fig. 1(c) and the corresponding density matrix is expressed as

$$\rho_{\text{PPS}} = \frac{1 - \kappa}{2^3} \mathbb{1}^{\otimes 3} + \kappa |000\rangle \langle 000|, \quad (13)$$

where κ is the thermal polarization factor (typically $\sim 10^{-5}$) at room temperature. The term $\mathbb{1}$ denotes the 2×2 identity operator. The PPS was experimentally reconstructed using the the least squares constrained convex optimization method [27] with a set of tomographic pulses $\{\mathbb{1}\mathbb{1}\mathbb{1}, \mathbb{1}\mathbb{1}R_y, \mathbb{1}R_yR_y, R_y\mathbb{1}\mathbb{1}, R_xR_yR_x, R_xR_xR_y, R_xR_xR_x\}$. Here $R_{x(y)}$ denotes a spin-selective $\pi/2$ rotation about the $x(y)$ axis. The fidelity of the experimentally reconstructed state ρ_{exp} with respect to the expected theoretical state ρ_{th} was evaluated using the Uhlmann-Jozsa fidelity measure [28, 29] as

$$\mathcal{F}(\rho_{\text{exp}}, \rho_{\text{th}}) = \left[\text{Tr} \left(\sqrt{\sqrt{\rho_{\text{th}}} \cdot \rho_{\text{exp}} \cdot \sqrt{\rho_{\text{th}}}} \right) \right]^2. \quad (14)$$

The average state fidelity of the experimentally reconstructed PPS was computed to be 0.9799 ± 0.0010 .

B. Experimental Simulation using the Duality Quantum Computing (DQC) Algorithm

Each Kraus operator \mathcal{K}_m corresponding to the quantum channel Λ (as in Eq. (2)) can be mapped to a decomposable operator \mathcal{L}_m using the unitary operator \tilde{U}_m as $\mathcal{K}_m = \tilde{U}_m \mathcal{L}_m$ [30]. Here, the index m labels the individual Kraus operators and is not summed over. The operator \mathcal{L}_m can be decomposed into a linear combination of at most d^2 unitary operators, U_j with complex coefficients β_j as $\mathcal{L}_m = \sum_{j=0}^{d^2-1} \beta_j^m U_j$. This decomposition enables the use of the duality quantum computing (DQC) framework, that allows the simulation of a sum of d^2 unitary operators acting on $\log_2 d$ qubits. The DQC framework achieves this using an ancillary system of at most $n = \log_2 d^2$ qubits [24, 31, 32]. Therefore, to simulate a quantum channel acting on a single qubit system, one requires a maximum of two ancillary qubits.

The steps in the DQC algorithm are delineated below.

- The system qubit is initialized in the desired input state $|\Phi\rangle$, while the ancillary system consisting of n qubits is initialized in the $|0\rangle^{\otimes n}$ state.

- Following this, a unitary operator V is implemented on the ancillary qubit and the joint state of the system and ancillary qubit, evolving the initial state as $|\Phi\rangle |0\rangle \rightarrow \sum_{j=0}^{d^2-1} |\Phi\rangle V_{j0} |j\rangle$. Here, V_{j0} represents the first column of the unitary matrix V , determined by the complex coefficients in the unitary expansion of the Kraus operator. The remaining columns of V are constructed using the Gram–Schmidt orthogonalization procedure to ensure unitarity.

- A controlled unitary operation $\sum_{j=0}^{d^2-1} U_j \otimes |j\rangle \langle j|$ is performed on the system qubit with the state of the ancillary qubit acting as control, which transforms the state as

$$\sum_{j=0}^{d^2-1} V_{j0} |\Phi\rangle |j\rangle \rightarrow \sum_{j=0}^{d^2-1} V_{j0} U_j |\Phi\rangle |j\rangle. \quad (15)$$

- Next, a unitary operation W is applied on the ancillary qubit, which leads to the state evolution

$$\sum_{m,j=0}^{d^2-1} W_{mj} V_{j0} U_j |\Phi\rangle |m\rangle = \sum_{m=0}^{d^2-1} \mathcal{L}_m |\Phi\rangle |m\rangle. \quad (16)$$

The elements of the matrix W are uniquely determined based on the choice of the unitary matrix V and are constructed such that the operator \mathcal{L}_m satisfies the relation $\mathcal{L}_m = \sum_{j=0}^{d^2-1} W_{mj} V_{j0} U_j$.

- An additional controlled unitary operation is implemented on the system qubit, with the state of the ancillary qubit as control, to map the operator \mathcal{L}_m to the Kraus operators \mathcal{K}_m . This transformation is expressed as

$$\sum_{m=0}^{d^2-1} \tilde{U}_m \mathcal{L}_m |\Phi\rangle |m\rangle = \sum_{m=0}^{d^2-1} \mathcal{K}_m |\Phi\rangle |m\rangle, \quad (17)$$

where, each Kraus operator is defined as $\mathcal{K}_m = \tilde{U}_m \sum_{j=0}^{d^2-1} W_{mj} V_{j0} U_j$. This step ensures that the full action of the quantum channel is implemented on the system qubit.

- In the final step, a measurement is performed on the ancillary system in the computational basis. Upon measuring the ancillary qubit in $|m\rangle$ state, we get the action of the Kraus operator \mathcal{K}_m simulated on the system qubit.

We now move towards the experimental demonstration of the recovery of a quantum state that has undergone decoherence due to a given damping channel—either PD or AD channel, using the Petz recovery map. In NMR systems, amplitude damping and phase damping correspond to intrinsic decoherence mechanisms characterized by the

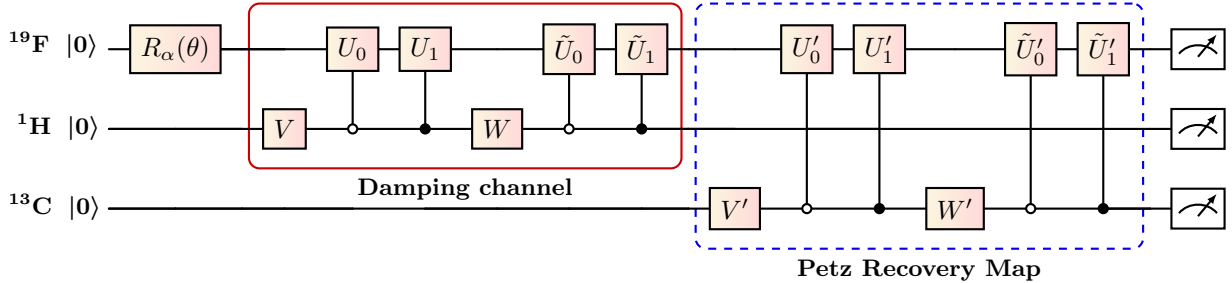


FIG. 2: (Color online) Schematic of the quantum circuit used to implement the damping channel and the corresponding Petz recovery map. The gate $R_\alpha(\theta)$ denotes a rotation by an angle θ about the $\alpha \in \{x, y, z\}$ axis, used to initialize the system qubit (^{19}F) in state $|\Phi\rangle$. The red solid rectangle denotes the segment of the circuit implementing the damping channel, comprising unitary gates V, W and controlled unitary operations U_0, U_1, \tilde{U}_0 , and \tilde{U}_1 . The Petz recovery map, shown within the blue dashed region, involves the unitaries V', W' and controlled unitaries U'_0, U'_1, \tilde{U}'_0 , and \tilde{U}'_1 . The specific forms of these unitaries differ depending on the channel (PD or AD) and are provided in Eqs. (19),(20), (21), and (22), respectively.

relaxation times T_1 and T_2 , respectively. In our simulations, these effects are modeled as ideal quantum channels applied explicitly to the system, rather than arising from the underlying physical noise naturally present in the NMR environment. This approach is also essential because the experimental implementation of the associated recovery maps requires explicit knowledge of the map itself. It must be noted that for the specific quantum channels considered in our study, a single ancillary qubit is sufficient to implement the desired channel dynamics, as the maps are of rank-2 (two canonical Kraus operators). By the same analogy, the simulation of the Petz recovery map associated with the corresponding damping channel also requires only one ancillary qubit.

In all the experiments, we consider ^{19}F as the system qubit and ^1H and ^{13}C as ancillary qubits to implement the damping channel and the corresponding Petz recovery map, respectively. The experimental protocol, beginning with the PPS is detailed below.

- The system and ancillary qubits are initialized in the state $|\Phi\rangle \otimes |00\rangle$ by applying the rotation gate $R_\alpha(\theta)$ on the system qubit; $R_\alpha(\theta)$ denotes a rotation about the axis $\alpha \in \{x, y, z\}$ by an angle θ .
- The damping channel is then implemented, followed by the corresponding Petz recovery map using the appropriate NMR pulse sequences.
- Finally, quantum state tomography is performed to reconstruct the output density matrix of the system qubit.

In NMR, seven tomography pulses are required to reconstruct the complete density matrix of a three-qubit system [33]. However, in our implementation, we are specifically interested in the final state of the system qubit alone. As described earlier, the structure of the DQC algorithm ensures that each Kraus operator acts within a distinct subspace of the ancillary qubit. Taking advantage of this structure, we reconstruct the state of the

system qubit by performing tomography using only a reduced set of pulses $\{\mathbb{1}\mathbb{1}\mathbb{1}, R_y\mathbb{1}\mathbb{1}\}$. The signal integrals obtained from these measurements are summed to yield the density matrix of the system qubit, which is mathematically equivalent to tracing out the ancillary qubits from the three-qubit density matrix.

The quantum circuit shown in Fig. 2, provides a general framework applicable to both the channels and their respective Petz recovery maps using the duality quantum algorithm. Within this framework, the simulation of each channel involves a specific set of unitary operators tailored to the Kraus decomposition of a quantum channel. We now proceed towards the unitary constructions and their corresponding pulse sequences for each channel.

C. Amplitude Damping (AD) Channel and the Associated Petz Recovery Map

To simulate the action of the AD channel using the duality quantum algorithm, we first express each Kraus operator in [Eq. (8)] as a linear combination of Pauli matrices as

$$\begin{aligned} \mathcal{K}_0^{AD} &= \frac{1 + \sqrt{1-p}}{2} \mathbb{1} + \frac{1 - \sqrt{1-p}}{2} Z \\ \mathcal{K}_1^{AD} &= \frac{\sqrt{p}}{2} X.(\mathbb{1} - Z). \end{aligned} \quad (18)$$

Based on this decomposition, we identify the unitary matrices V, W, U_j and \tilde{U}_j as

$$\begin{aligned} U_0 &= \mathbb{1}, & U_1 &= Z, & \tilde{U}_0 &= \mathbb{1}, & \tilde{U}_1 &= X, \\ V = W &= \begin{pmatrix} \sqrt{\frac{1+\sqrt{1-p}}{2}} & \sqrt{\frac{1-\sqrt{1-p}}{2}} \\ \sqrt{\frac{1-\sqrt{1-p}}{2}} & -\sqrt{\frac{1+\sqrt{1-p}}{2}} \end{pmatrix} \end{aligned} \quad (19)$$

where, $\mathbb{1}$ is the 2×2 Identity operator and X, Z represents Pauli- x, z matrices respectively. Following Eq. (17), we

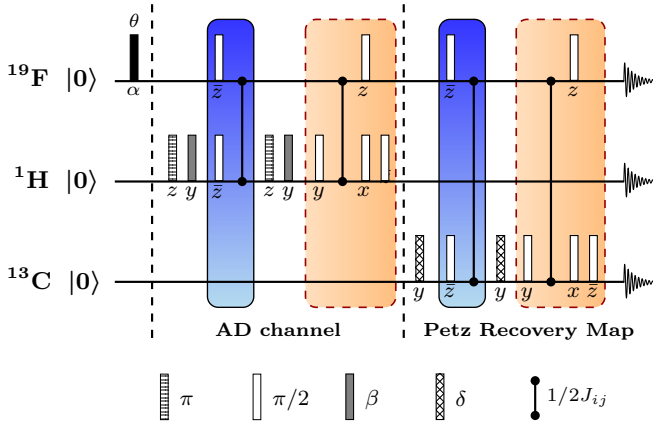


FIG. 3: (Color online) NMR pulse sequence used to realize the recovery of a quantum state $|\Phi\rangle$, undergoing decoherence by the AD channel using the Petz recovery map. A single-qubit rotation $R_\alpha(\theta)$ along axis $\alpha \in \{x, y, z\}$ with angle θ is applied to initialize the system qubit ^{19}F in the desired state $|\Phi\rangle$. Pulse phases are written beneath each rectangle, with an overbar indicating negative phase. The angles β and δ are given by $\beta = 2 \cos^{-1} \sqrt{\frac{1+\sqrt{1-p}}{2}}$ and $\delta = 2 \cos^{-1} \sqrt{\frac{1+c}{2}}$ with $c = \sqrt{\frac{1-\epsilon}{1-(1-p)\epsilon}}$. The pulse sequence enclosed within the solid box shaded blue, corresponds to a control- Z operation, while the sequence within the dashed box shaded orange, represents the control-NOT operations.

infer that the duality algorithm encodes the action of each Kraus operator within orthogonal subspaces of the ancillary qubit. For instance, the action of the Kraus operator \mathcal{K}_0^{AD} is simulated within the $|0\rangle$ sub-space of ancillary qubit, while \mathcal{K}_1^{AD} is simulated in $|1\rangle$ subspace.

To implement the Petz recovery map with reference state $\sigma = (1 - \epsilon)|0\rangle\langle 0| + \epsilon|1\rangle\langle 1|$, we find that the associated unitaries U'_0 , U'_1 , \tilde{U}'_0 and \tilde{U}'_1 are the same as U_0 , U_1 , \tilde{U}_0 and \tilde{U}_1 respectively as in Eq. (19). The unitaries V' and W' appearing in the Petz recovery stage transform as

$$V' = W' = \begin{pmatrix} \sqrt{\frac{1+c}{2}} & \sqrt{\frac{1-c}{2}} \\ -\sqrt{\frac{1-c}{2}} & \sqrt{\frac{1+c}{2}} \end{pmatrix}, \quad (20)$$

where $c = \sqrt{\frac{1-\epsilon}{1-(1-p)\epsilon}}$.

D. Phase Damping (PD) Channel and the Corresponding Petz Recovery Map

Following the same procedure as for the AD channel, we implement the PD channel using the DQC algorithm. The Kraus operators are expressed as linear combinations

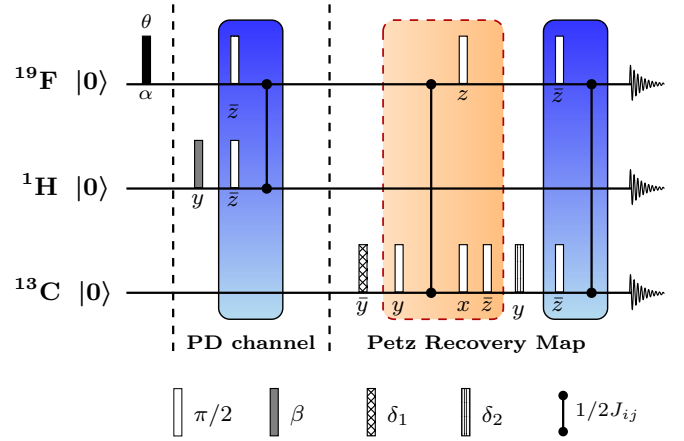


FIG. 4: (Color online) NMR pulse sequence to implement a PD channel and the Petz recovery map on quantum state $|\Phi\rangle$ undergoing decoherence under a PD channel using the Petz recovery map. The system qubit ^{19}F is initialized in the desired state $|\Phi\rangle$ by applying a single-qubit rotation $R_\alpha(\theta)$ along the axis $\alpha \in \{x, y, z\}$ with an angle θ . The angles β , δ_1 and δ_2 are defined as

$$\beta = 2 \sin^{-1} \sqrt{\frac{\rho}{2}} \text{ and } \delta_1 = 2 \cos^{-1} \sqrt{\lambda_+^2 + \mu_+^2} \text{ and}$$

$$\delta_2 = 2 \sin^{-1} \sqrt{\lambda_-^2 + \mu_-^2}.$$

Colored segments indicate two-qubit operations. The solid rectangular box highlighted in blue indicates the sequence implementing a control- Z operation, while the dashed rectangular box shaded in orange denotes the sequence corresponding to a control-NOT operation.

of Pauli matrices leading to the following unitaries:

$$U_0 = \mathbb{1}, \quad U_1 = Z, \quad \tilde{U}_0 = \mathbb{1}, \quad \tilde{U}_1 = \mathbb{1}, \quad (21)$$

$$V = \begin{pmatrix} \sqrt{1 - \frac{p}{2}} & -\sqrt{\frac{p}{2}} \\ \sqrt{\frac{p}{2}} & \sqrt{1 - \frac{p}{2}} \end{pmatrix}, \quad W = \mathbb{1}.$$

To implement the Petz map with reference state, $\sigma = (1-\epsilon)|+\rangle\langle+| + \epsilon|-\rangle\langle-|$, we obtain the following unitaries

$$U'_0 = \mathbb{1}, \quad U'_1 = X, \quad \tilde{U}'_0 = \mathbb{1}, \quad \tilde{U}'_1 = Z, \\ V' = \begin{pmatrix} \sqrt{\lambda_+^2 + \mu_+^2} & \sqrt{1 - \lambda_+^2 - \mu_+^2} \\ -\sqrt{1 - \lambda_+^2 - \mu_+^2} & \sqrt{\lambda_+^2 + \mu_+^2} \end{pmatrix}, \quad (22) \\ W' = \begin{pmatrix} \sqrt{1 - \lambda_-^2 - \mu_+^2} & -\sqrt{\lambda_-^2 + \mu_+^2} \\ \sqrt{\lambda_-^2 + \mu_+^2} & \sqrt{1 - \lambda_-^2 - \mu_+^2} \end{pmatrix}$$

where λ_{\pm} and μ_{\pm} are defined in Eq. (11). As before, $\mathbb{1}, X, Z$ represent the identity and Pauli operators, respectively. For the Petz recovery map for PD channel, the decomposition of the Kraus operator $\mathcal{M}_1^{PD} = Z.(\mu_+\mathbb{1} + \mu_-X)$, involves a product with the Pauli- z operator. Consequently, a controlled- Z gate is implemented as controlled \hat{U}'_1 .

The NMR pulse sequences for implementing the AD and PD channels, along with their respective Petz re-

covery maps, are shown in Figs. 3 and 4, respectively. Each sequence is divided into three segments: the initialization segment, which prepares the qubit ^{19}F in state $|\Phi\rangle$ via a single-qubit rotation; the damping channel segment, which simulates the decoherence process; and the recovery segment, which implements the Petz recovery map.

IV. RESULTS AND DISCUSSION

To experimentally demonstrate quantum state recovery under a damping channel using the Petz recovery map, we performed two sets of experiments for each input state. In the first set, the system qubit was subjected to the damping channel (either AD or PD) only. In the second set, following the application of the damping channel, the associated Petz recovery map was implemented using the NMR pulse sequence depicted in Figs. 3 and 4. In addition, the recovery experiments were repeated for different values of the reference state parameter ϵ . To evaluate the performance of recovery, we compared the fidelity of both the damped state and the recovered state with respect to the original input state of the system qubit, and plotted it as a function of the strength of the damping channel.

Fig. 5 depicts the experimental results for the AD channel and its corresponding Petz recovery map. For the experimental implementation, we consider the system qubit initialized in different input states: $|0\rangle$, $|1\rangle$, $|+\rangle = \frac{|0\rangle+|1\rangle}{\sqrt{2}}$ and $0.9268|0\rangle+0.3754i|1\rangle$. The reference state for constructing the Petz map was chosen to be of diagonal form, $\sigma = (1 - \epsilon)|0\rangle\langle 0| + \epsilon|1\rangle\langle 1|$, and recovery was performed for three different values of $\epsilon = 0.2, 0.5, 0.8$. The plots in the panels (a) and (b), illustrate that under the AD channel, the fidelity for the $|0\rangle$ state remains one as expected, since the AD process drives the system towards the $|0\rangle$ state. Conversely, the $|1\rangle$ state experiences significant decoherence. On implementing the Petz recovery map, the fidelity of the recovered state with respect to the $|0\rangle$ state decreases, while the fidelity with respect to the $|1\rangle$ state increases, with increase in ϵ . This behavior reflects the dependence of the Petz recovery map on the choice of reference state. For an input state $|0\rangle$, the most suitable reference is one that is close to $|0\rangle$ itself i.e. smaller values of ϵ . As ϵ increases, the reference state shifts toward $|1\rangle$. Thus, for the initial state $|1\rangle$, higher values of ϵ are more appropriate. Panels (c) and (d) display the results for the $|+\rangle$ and $0.9258|0\rangle+0.3781i|1\rangle$ states. Both these states exhibit behaviors similar to the $|0\rangle$ state. However, the fidelity loss for the $|+\rangle$ state is less as compared to the $|0\rangle$ state. This occurs because the $|+\rangle$ state is an equal superposition of the $|0\rangle$ and $|1\rangle$ states. As a result, the coherence reduces in magnitude, but the state does not completely collapse to $|0\rangle$. For this state as well, a smaller ϵ is the better choice.

The experimental fidelity results for system qubit subjected to phase damping channel and its Petz recovery

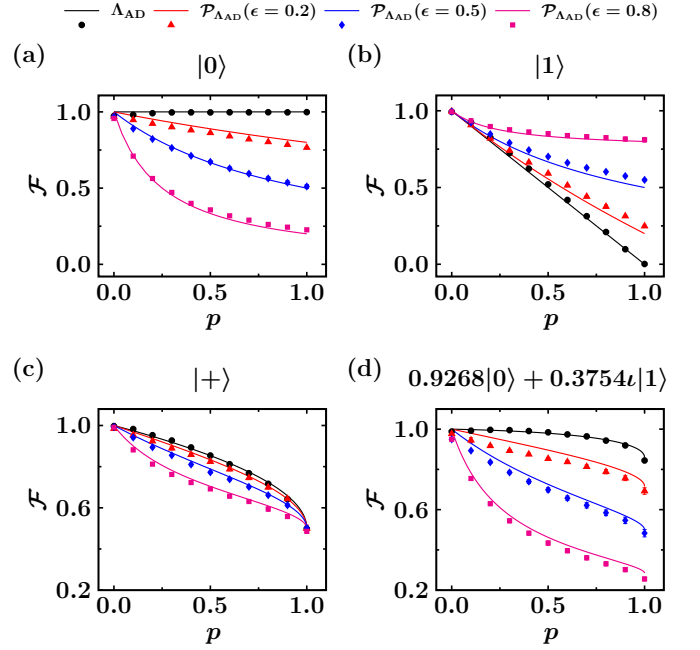


FIG. 5: (Color online) Experimental results for the AD channel (black circles) and the corresponding Petz recovery map implemented using the DQC algorithm. The recovery map is constructed with reference states of the form $\sigma = (1 - \epsilon)|0\rangle\langle 0| + \epsilon|1\rangle\langle 1|$, for various ϵ values. Plots in panels (a), (b), (c) and (d) depict fidelity \mathcal{F} as a function of AD channel strength p , for initial states $|0\rangle, |1\rangle, |+\rangle = \frac{|0\rangle+|1\rangle}{\sqrt{2}}$ and $0.9268|0\rangle + 0.3754i|1\rangle$, respectively. Red triangles, blue diamonds and magenta squares represent experimental fidelities after applying the Petz recovery map with $\epsilon = 0.2, 0.5$ and 0.8 , respectively. The solid lines depict the corresponding theoretical behavior. The size of the statistical error bars are smaller than the marker size, and are therefore not visible.

map are depicted in Fig. 6. In this case, we initialize our system qubit in different input states: $|\pm\rangle = \frac{|0\rangle\pm|1\rangle}{\sqrt{2}}$, $|0\rangle$ and $0.9268|0\rangle + 0.3754i|1\rangle$. The Petz map is constructed using reference state $\sigma = (1 - \epsilon)|+\rangle\langle +| + \epsilon|-\rangle\langle -|$. The experiment is repeated for three different values of $\epsilon = 0.2, 0.5, 0.8$. As highlighted in the previous paragraph, the performance of the Petz map in recovering the damped state strongly depends on the choice of reference state. This behavior under the PD channel is shown in the plots in the panels (a) and (b) of Fig. 6. When ϵ is small, for e.g. $\epsilon = 0.2$, the reference lies closer to state $|+\rangle$ and away from state $|-\rangle$. With this choice of reference state parameter, fidelity of the recovered state increases and we get efficient recovery for the input state $|+\rangle$. In contrast, the fidelity decreases for the input state $|-\rangle$ (red triangle and red solid line in plots (a) and (b) respectively). Conversely, $\epsilon = 0.8$, the reference state moves away from the $|+\rangle$ state and shift towards $|-\rangle$ state. This improves the fidelity for the input state $|-\rangle$,

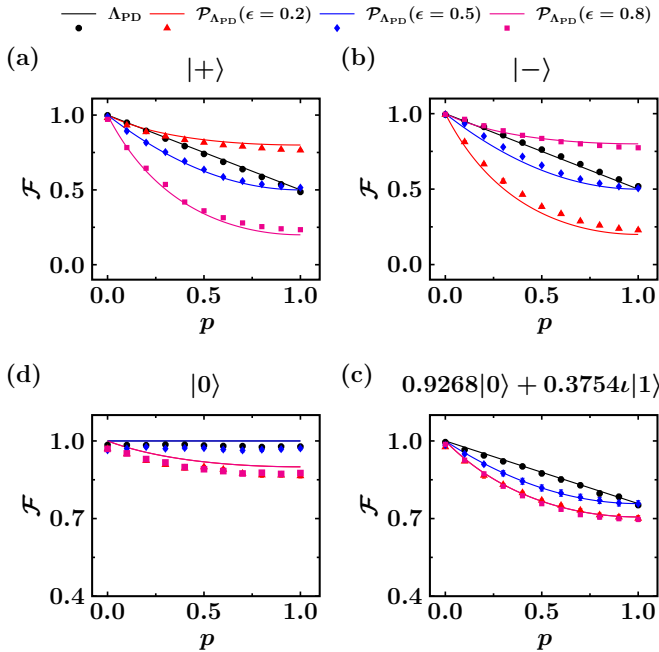


FIG. 6: (Color online) Experimental results showing the effect of the PD channel and the corresponding Petz recovery map implemented via the DQC algorithm. The Petz recovery map is designed using reference states of the form $\sigma = (1 - \epsilon)|+\rangle\langle+| + \epsilon|-\rangle\langle-|$, for various ϵ values, where $| \pm \rangle$ are eigen states of Pauli- x operator. Plots in panels (a), (b), (c) and (d) depict fidelity \mathcal{F} as a function of PD channel strength p , for different initial states: $|+\rangle$, $|-\rangle$, $|0\rangle$ and $0.9268|0\rangle + 0.3754i|1\rangle$, respectively. Black circles represent fidelity after phase damping, while red triangles, blue diamonds and magenta squares show the fidelity after implementing the Petz recovery map with $\epsilon = 0.2, 0.5$ and 0.8 , respectively. Theoretical predictions are indicated by solid lines. Statistical error bars are smaller than the marker size and are hence not visible in the plots.

while reducing fidelity for the input state $|+\rangle$ (magenta square and magenta solid line in plots (a) and (b) respectively). Interestingly, for $\epsilon = 0.5$, the reference state becomes maximally mixed, leading to no recovery for both the input states. This is due to the fact that the PD channel specifically affects the off-diagonal elements of the density matrix, and the corresponding Petz map in this case is itself a PD channel. As a result, instead of improving the recovery, the map further reduces the fidelity of the recovered state. For input states $|0\rangle$ and $0.9268|0\rangle + 0.3754i|1\rangle$, the corresponding experimental results are shown in panels (c) and (d), respectively. In case of $|0\rangle$ input state, recovery is not observed for any value of ϵ except $\epsilon = 0.5$. This behavior arises because both the input and the chosen reference state in this case are diagonal in the computational basis, and the

PD channel affects only the off-diagonal elements. Although the input state $0.9268|0\rangle + 0.3754i|1\rangle$ is closer in amplitude to the $|0\rangle$ state, the reference states used in constructing the Petz map (based on $|+\rangle$ and $|-\rangle$) are not well suited for recovering this particular input state. As a result, no significant recovery is observed for any of the ϵ values considered.

V. CONCLUSIONS

We have experimentally investigated the performance of the Petz recovery map in retrieving the quantum state of a single qubit undergoing amplitude damping and phase damping on an NMR quantum information processor. By initializing the qubit in different input states and implementing both channels and their associated Petz recovery maps via the duality quantum computing algorithm, we analyzed how recovery fidelity depends on the choice of the reference state used in the construction of the Petz map. Our results show that the performance of recovery is highly sensitive to the overlap between the input state and the reference state. For the AD channel, we employed a diagonal reference state. Since the AD channel naturally drives any input state towards the $|0\rangle$ state, the recovery map was found to be most effective for the $|1\rangle$ state for all choices of the input state that we considered. In contrast, for the PD channel, we used a reference state that is in a parameterized superposition of $|+\rangle$ and $|-\rangle$ states. In this case, the recovery fidelity for the input state (for e.g. $|+\rangle$) improves with increasing overlap with the reference state, while it decreases for the orthogonal one (for e.g. $|-\rangle$), under the same conditions.

Our experimental implementation of the Petz recovery map on an NMR quantum processor demonstrates its feasibility in a controlled, real-world setting and confirms key theoretical predictions regarding its dependence on the reference state. It shows how the Petz map can be tailored to specific noise channels, opening new avenues for exploring quantum error correction and noise mitigation in near-term quantum devices. Future work will extend these results to multi-qubit systems, more complex noise models and integration with fault-tolerant schemes.

ACKNOWLEDGMENTS

All experiments were performed on a Bruker Avance-III 600 MHz FT-NMR spectrometer at the NMR Research Facility at IISER Mohali. G.S. acknowledges University Grants Commission (UGC), India, for financial support. N.K.B. acknowledges financial support from CNPq Brazil (442429/2023-1) and FAPESP (Grant 2021/060350). N.K.B. is part of the Brazilian National Institute for Quantum Information (INCT Grant 465469/2014-0).

[1] E. B. Davies, *Quantum theory of open systems* (Academic Press, San Diego, CA, 1976).

[2] S. Haroche and J.-M. Raimond, *Exploring the Quantum: Atoms, Cavities, and Photons* (Oxford University Press, Oxford, 2006).

[3] I. L. Chuang, R. Laflamme, P. W. Shor, and W. H. Zurek, *Science* **270**, 1633 (1995).

[4] P. W. Shor, *Phys. Rev. A* **52**, R2493 (1995).

[5] H. Aschauer and H. J. Briegel, in *Coherent Evolution in Noisy Environments*, Lecture notes in physics (Springer Berlin Heidelberg, Berlin, Heidelberg, 2002) pp. 235–261.

[6] Y. Matsuzaki, S. C. Benjamin, and J. Fitzsimons, *Phys. Rev. A* **84** (2011).

[7] T. Albash and D. A. Lidar, *Phys. Rev. A* **91** (2015).

[8] M. Schlosshauer, *Decoherence and the quantum-to-classical transition* (Springer, Berlin, Germany, 2007).

[9] L. M. K. Vandersypen and I. L. Chuang, *Rev. Mod. Phys.* **76**, 1037 (2005).

[10] H. Singh, Arvind, and K. Dorai, *Pramana - J. Phys.* **94** (2020).

[11] L. Deslauriers, S. Olmschenk, D. Stick, W. K. Hensinger, J. Sterk, and C. Monroe, *Phys. Rev. Lett.* **97**, 103007 (2006).

[12] D. Petz, *Commun. Math. Phys.* **105**, 123 (1986).

[13] D. Petz, *Rev. Math. Phys.* **15**, 79 (2003).

[14] H. Barnum and E. Knill, *J. Math. Phys.* **43**, 2097 (2002).

[15] H. K. Ng and P. Mandayam, *Phys. Rev. A* **81** (2010).

[16] C. C. Aw, F. Buscemi, and V. Scarani, *AVS Quantum Sci.* **3**, 045601 (2021).

[17] H. Kwon, R. Mukherjee, and M. S. Kim, *Phys. Rev. Lett.* **128**, 020403 (2022).

[18] J. Surace and M. Scandi, *Quantum* **7**, 990 (2023).

[19] W.-H. Png and V. Scarani, “Petz recovery maps of single-qubit decoherence channels in an ion trap quantum processor,” (2025), arXiv:2504.20399 [quant-ph].

[20] A. Gilyén, S. Lloyd, I. Marvian, Y. Quek, and M. M. Wilde, *Phys. Rev. Lett.* **128**, 220502 (2022).

[21] D. Biswas, G. M. Vaidya, and P. Mandayam, *Phys. Rev. Res.* **6** (2024).

[22] L. Lautenbacher, F. de Melo, and N. K. Bernardes, *Phys. Rev. A* **105** (2022).

[23] L. Lautenbacher, V. Jagadish, F. Petruccione, and N. K. Bernardes, *Phys. Lett. A* **512**, 129583 (2024).

[24] T. Xin, S.-J. Wei, J. S. Pedernales, E. Solano, and G.-L. Long, *Phys. Rev. A* **96**, 062303 (2017).

[25] V. Jagadish and F. Petruccione, *Quanta* **7**, 54 (2018).

[26] I. S. Oliveira, T. J. Bonagamba, R. S. Sarthour, J. C. Freitas, and E. R. deAzevedo, in *NMR Quantum Information Processing* (Elsevier Science B.V., Amsterdam, 2007) pp. 137–181.

[27] A. Gaikwad, Arvind, and K. Dorai, *Quant. Inf. Proc.* **20**, 19 (2021).

[28] A. Uhlmann, *Rep. Math. Phys.* **9**, 273 (1976).

[29] R. Jozsa, *J. Mod. Opt.* **41**, 2315 (1994).

[30] S.-J. Wei, T. Xin, and G.-L. Long, *Sci. China Phys. Mech. Astron.* **61**, 70311 (2018).

[31] V. Gulati, V. Jagadish, R. Srikanth, and K. Dorai, *Phys. Rev. A* **109**, 042419 (2024).

[32] G. Singh, A. Gaikwad, Arvind, and K. Dorai, “Experimental decoherence mitigation using a weak measurement-based scheme and the duality quantum algorithm,” (2024), arXiv:2409.12752 [quant-ph].

[33] G. M. Leskowitz and L. J. Mueller, *Phys. Rev. A* **69**, 052302 (2004).